World Scientific
www.worldscientific.com

Linear energy stable methods for an epitaxial growth model with slope selection

Gregory M. Seyfarth

*Department of Physics and Astronomy, Colby College
Waterville, Maine 04901, USA
greg.516@gmail.com*

Benjamin Vollmayr-Lee*

*Department of Physics and Astronomy, Bucknell University
Lewisburg, Pennsylvania 17837, USA
bvollmay@buckhell.edu*

We consider a phase field model for molecular beam epitaxial growth with slope selection with the goal of determining linear energy stable time integration methods for the dynamics. Stable methods for this model have been found via a concave-convex splitting of the dynamics, but this approach generally leads to a nonlinear update equation. We seek a linear energy stable method to allow for simple and efficient time marching with fast Fourier transforms. Our approach is to parametrize a class of semi-implicit methods and perform unconditional von Neumann stability analysis to identify the region of stability in parameter space. Since unconditional von Neumann stability does not ensure energy stability, we perform extensive numerical tests and find strong agreement between the predicted and observed stable regions of parameter space. This analysis elucidates a novel feature that the stability region in parameter space differs for a mono-domain system (single equilibrium slope) versus a many-domain system (coarsening facets from an initially flat surface). The utility of these steps is then demonstrated by a comparison of the coarsening dynamics for isotropic and anisotropic variants of the model.

Keywords: Epitaxial crystal growth; coarsening; energy stability; unconditional von Neumann stability.

PACS Nos.: 11.25.Hf, 123.1K.

1. Introduction

In growing crystal surfaces by molecular beam epitaxy (MBE), the Ehrlich–Schwoebel–Villain effect[1–3] can destabilize a flat interface and lead to the formation of pyramids or mounds (see Ref. 4 for a recent review). These surface features then coarsen, with their height and spatial extent growing as powers of time. Theoretical

*Corresponding author.

studies of MBE coarsening typically employ continuum models with nonlinear equations of motion. Unfortunately, numerical integration of these equations is hampered by instabilities. As such, much recent effort has been devoted to finding stable integration methods. In this work, we determine a class of linear energy stable integration methods that are particularly efficient and simple to implement because the updated field can be obtained via the fast Fourier transform (FFT).

Our model consists of a height field $h(x, y, t)$ that obeys the equation of motion

$$\frac{\partial h}{\partial t} = -\varepsilon^2 \nabla^4 h - \nabla \cdot \{(1 - |\nabla h|^2)\nabla h\}, \tag{1}$$

applicable for homoepitaxial growth with isotropic slope selection. The motivation for this and related models is discussed below. With these dynamics, equilibrated regions of uniform gradient and unit slope form. Domains with different slope orientations meet at edges of constant width w, which is of order ε. As the system evolves the edges are healed out, resulting in the growth of the characteristic domain size $L(t)$. For this particular model, the power law growth $L(t) \sim t^{1/3}$ has been found from theoretical analysis,[5–8] simulations,[6,7,9] and rigorous bounds.[10]

Numerical simulations of coarsening are useful for testing scaling and the predicted growth laws and for measuring properties of the scaling state, such as correlations, growth law amplitudes, autocorrelation functions, and more (see Ref. 11 for a coarsening review). But these simulations face several restrictions. To reach the asymptotic scaling regime, it is necessary to evolve until the domain size is much greater than the edge width, $L(t) \gg w$. But the lattice size Δx must be sufficiently small compared to w, in order to resolve the edge shape and corresponding line tension. Finally, the system size L_{sys} must be large enough that domains can grow into the scaling regime before finite size effects appear. To satisfy this string of conditions, $\Delta x < w \ll L(t) \ll L_{\text{sys}}$, requires lattices of very large linear size $L_{\text{sys}}/\Delta x$, evolved to late times.

Thus, for coarsening studies it is crucial to use integration schemes that are *accuracy*-limited rather than *stability*-limited. The order of the accuracy and the size of the truncated error is relatively less important. The distinction is that stability-limited methods require marching with a fixed-size time step, while an unconditionally stable method, i.e. one with no conditions on Δt, allows a time step determined by the natural time scale of the dynamics. Since the characteristic edge velocity scales as $v_{\text{edge}} \sim \partial L/\partial t \sim t^{-2/3}$, where t is the instantaneous time, this allows a *growing* time step $\Delta t \sim At^{2/3}$ (see Refs. 12, 13). The order of the method and the size of the truncation error affect the optimal choice of the coefficient A, but do not alter the time exponent. Using $dt/dn \sim \Delta t$, where n is the number of integration steps, it follows that unconditionally stable methods allow accurate evolution with $t \sim n^3$, rather than the stability-limited $t \sim n$. For typical simulation parameters, this provides greater than a 1000-fold increase in efficiency!

Eyre provided a general approach for generating unconditionally stable semi-implicit integration methods, based on a convex-concave splitting.[14] These schemes

are *energy stable*, which means they preserve the monotonic energy decrease of the continuous time equation. This convex-concave splitting has been successfully applied to Eq. (1),[9,15–17] but these schemes have nonlinear implicit terms that require iteration to solve for the updated field. Qiao, Sun, and Zhang constructed *linear* energy stable methods,[18] but their implicit terms contain nonconstant, field-dependent factors, so the update equation must similarly be solved iteratively rather than directly by FFT.

Our goal is to find integration methods for Eq. (1) that are (i) unconditionally energy stable, i.e. stable for any size time step Δt, and (ii) linear in the updated field with constant coefficients, so the updated field can be obtained directly via FFT. Such methods were found for a model of MBE growth without slope selection.[19,20] For the model with slope selection, Xu and Tang proved that a scheme with both properties is possible, given an assumption that the magnitude of the slope $|\nabla h|$ has an upper bound.[21] Our work is complementary to Ref. 21 in ways we will describe below.

Our method is to parametrize steps with linear implicit terms that can be solved directly by FFT, determine the range of step parameters that satisfy unconditional von Neumann (UvN) stability, and then test these parameters numerically for energy stability. This approach yielded stable, direct steps for the Cahn–Hilliard and Allen–Cahn equations.[12] We find for the equation of motion, Eq. (1), there exists a class of first-order, semi-implicit steps

$$
\begin{aligned}
h_{t+\Delta t} = h_t + \Delta t[-\varepsilon^2 \nabla^4 h_t - \nabla \cdot \{(1 - |\nabla h_t|^2)\nabla h_t\}] \\
- b_1 \Delta t \nabla^2 (h_{t+\Delta t} - h_t) - b_2 \varepsilon^2 \Delta t \nabla^4 (h_{t+\Delta t} - h_t)
\end{aligned} \tag{2}
$$

that provides stable numerical integration for appropriate choice of the parameters b_1 and b_2, as shown in Fig. 1. The b_1 and b_2 terms are added for stability purposes and are the same order as the error. The results of our UvN stability analysis are presented as shaded regions while our numerical tests of energy stability are plotted as points. Although UvN stability does not ensure energy stability, we find that it is very effective in determining the energy stable regions.

The UvN stability conditions plotted here are independent of lattice type or details of the spatial derivatives (e.g. finite difference versus spectral methods), relying only on the negative semi-definite spectrum of the laplacian. In comparison to Xu and Tang,[21] the current work provides the following:

(a) Xu and Tang proved energy stability for the parameters $b_1 < -1$ and $b_2 = 1$. While we lack a proof and rely on numerical confirmation, our results are consistent with theirs and extend the stable parameter range to all $b_2 > 1/2$.

(b) The UvN stability analysis and our numerical tests reveal an interesting feature: the stability range differs for single- and many-domain systems. The analysis shows that the most unstable Fourier mode is that with its wavevector oriented with the local slope ∇h. In the many-domain system, of interest in coarsening studies, each mode samples many different slope directions, which acts to suppress the instability. This expands the stable parameter range to $b_1 < -1/2$.
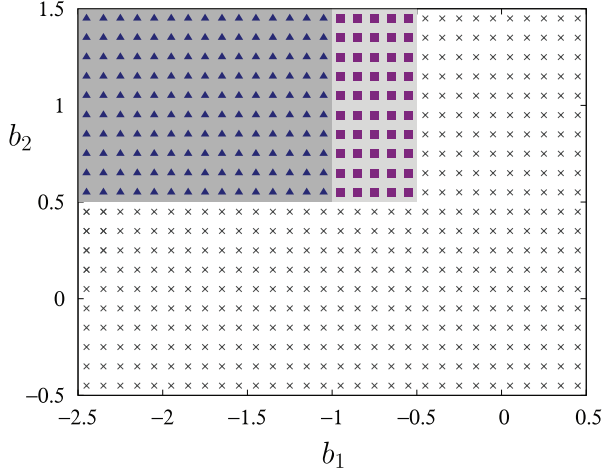
Fig. 1. (Color online) Stability diagram for the parameters b_1 and b_2 in Eq. (2). The UvN stable parameter values are shaded in gray, with the darker region corresponding to a single-domain system and the combined gray regions corresponding to a many-domain system. The points represent numerical tests of energy stability: the (blue) triangles are parameter values that are stable for single-domain systems; these together with the (purple) squares are stable for multi-domain systems; and the $\times$ are parameter values that were found to be unstable.

(c) We perform extensive numerical tests, building on the testing done in Refs. 7, 21. This is important for supporting the assumption present in both Xu-Tang and the present work that the slope $|\nabla h|$ may safely be assumed to be bounded.

(d) We find, in conjunction with Ref. 12, a pattern of success for UvN stability analysis predicting the parameter range of energy stable methods. This is noteworthy because it is a relatively straightforward procedure that can be easily brought to new phase field models to develop more linear energy stable methods.

(e) As with Xu and Tang, our results can be generalized straightforwardly to anisotropic growth, where only a discrete set of slope orientations is preferred. We demonstrate this explicitly for a model with square symmetry, appropriate for growth on (100) surface. An application taking full advantage of the accuracy restriction yields the most extensive (to date) demonstration of power law growth, and challenges recent claims[8] that the square symmetry model should exhibit asymptotically $t^{1/3}$ growth.

The remainder of the paper is as follows. In Sec. 2, we review some of the properties of the model to provide necessary background for subsequent sections. In Sec. 3, we present the UvN stability analysis, both for single- and many-domain systems. We describe the numerical tests of energy stability in Sec. 4, and in Sec. 5 we extend our analysis to the anisotropic model with square symmetry. Details of our finite difference scheme are presented in Sec. 6, followed by the application of comparing the

asymptotic coarsening of the isotropic and square symmetry model in Sec. 7. Finally, we summarize our results in Sec. 8.

2. The Continuous Time Model

In this section, we provide motivation for the model and present some of its properties, showing in particular the instability to pyramid formation and the energy decreasing dynamics of the continuous time model.

The height field, $h(x, y, t)$, is defined in a co-moving frame so that its average is zero, and obeys a continuity equation. The current $\mathbf{J}$ has an equilibrium surface diffusion contribution equal to the gradient of the local curvature,[22] $\mathbf{J}_{\mathrm{SD}} = \nabla(\varepsilon^2 \nabla^2 h)$, and a nonequilibrium component $\mathbf{J}_{\mathrm{NE}}$:

$$\frac{\partial h}{\partial t} = -\nabla \cdot \mathbf{J} = -\varepsilon^2 \nabla^4 h - \nabla \cdot \mathbf{J}_{\mathrm{NE}}. \tag{3}$$

A noise term is omitted as this is considered to be irrelevant for coarsening.[11] We consider the slope-selecting nonequilibrium current

$$\mathbf{J}_{\mathrm{NE}} = (1 - |\nabla h|^2) \nabla h, \tag{4}$$

which gives $\mathbf{J}_{\mathrm{NE}} \sim \nabla h$ for small gradients, an uphill current due to the Ehrlich–Schwoebel–Villain effect,[3] and $\mathbf{J}_{\mathrm{NE}} = 0$ for slopes of unit magnitude. Inserting Eq. (4) into the continuity Eq. (3) yields the equation of motion, Eq. (1).

Common variations on this model include slope-selecting currents that vanish for only a discrete set of ∇h directions, reflecting the underlying crystalline structure, and models without slope selection. The physical basis and experimental evidence for these various models are described in Refs. 5, 6, 23–25 and references therein.

The equation of motion, Eq. (1), can be written as a gradient flow

$$\frac{\partial h}{\partial t} = -\frac{\delta F}{\delta h} \tag{5}$$

for the free energy functional

$$F[h] = \int d^2 x \left\{ \frac{1}{2} \varepsilon^2 (\nabla^2 h)^2 + \frac{1}{4} (1 - |\nabla h|^2)^2 \right\}. \tag{6}$$

Gradient flow results in a monotonically decreasing free energy,

$$\frac{d}{dt} F = \int d^2 x \left(\frac{\delta F}{\delta h} \right) \frac{\partial h}{\partial t} = -\int d^2 x \left(\frac{\partial h}{\partial t} \right)^2 \leq 0. \tag{7}$$

As first noted by Eyre,[14] the essential stability criterion for discrete time steps is to preserve the energy decreasing property of the continuous time equation.

Next, we review the linear stability of the continuous time equation, which will be useful context for the von Neumann (VN) stability analysis in Sec. 3. Consider a height field

$$h(x, y, t) = Cx + \eta(x, y, t), \tag{8}$$

which consists of small deviations η from a uniform slope. Inserting this into Eq. (1), linearizing in η, and Fourier transforming to $\tilde{\eta}(\mathbf{k}, t) \equiv \int d^2x \exp(i\mathbf{k} \cdot \mathbf{x})\eta(x, y, t)$ gives

$$\frac{\partial \tilde{\eta}(\mathbf{k}, t)}{\partial t} = (k^2 - \varepsilon^2 k^4 - C^2 k^2 - 2C^2 k_x^2)\, \tilde{\eta}(\mathbf{k}, t). \tag{9}$$

For an interface that is initially flat we set $C = 0$ and obtain the growth rate for small fluctuations in the initial conditions:

$$\frac{\partial \tilde{\eta}(\mathbf{k}, t)}{\partial t} = k^2(1 - \varepsilon^2 k^2)\, \tilde{\eta}(\mathbf{k}, t). \tag{10}$$

Long wavelength modes with $k < \varepsilon^{-1}$ are unstable and grow, which is exactly the instability that leads to pyramid formation. In the context of the Cahn–Hilliard equation, this is the spinodal instability.[11] Note that the exponential growth of the mode is nevertheless accompanied by a decreasing total free energy, as required by Eq. (7).

For an equilibrium interface, we set the slope $C = 1$ to obtain

$$\frac{\partial \tilde{\eta}(\mathbf{k}, t)}{\partial t} = -(\varepsilon^2 k^4 + k_x^2)\, \tilde{\eta}(\mathbf{k}, t). \tag{11}$$

The negative right-hand side indicates that height fluctuations about the equilibrium slope decay, and the uniform slope profile is stable.

3. UvN Stability Analysis

The goal in constructing a discrete time method is to be faithful to the physical behavior of the continuous time equation. In our case, this means our discrete step should be energy stable to preserve the energy-decreasing property of the continuous equation. However, in this section, we analyze instead the vN stability, i.e. the linear stability of the discrete step, Eq. (2). This analysis has certain advantages. It is relatively straightforward and, as shown in Fig. 1 and in Ref. 12, it successfully predicts the parameter range for energy stability, as judged by numerical tests. Also, the method provides insight into the dynamics of the Fourier modes, which in the present case proves useful in clarifying the distinction between the single- and many-domain systems.

We first present vN stability analysis on the Euler step as an example with conditional stability, i.e. a lattice-dependent upper bound on Δt. Then we consider our parametrized semi-implicit step and perform UvN stability analysis; that is, we seek parameter values which yield vN stable steps for any size Δt. Note that we will only impose vN stability on the equilibrium, sloped interface and not on the flat interface, where the linear instability is part of the physical behavior of the continuum equation.

In addition to the time discretization, the spatial derivatives in our equation of motion must be treated by finite-difference or spectral methods. Without specifying

the details of the scheme, we denote the Fourier transform of the two-dimensional numerical laplacian as $\lambda(\mathbf{k})$. In the continuum limit, $\lambda(\mathbf{k}) \to -k^2$. For spatially discretized systems, $0 \geq \lambda(\mathbf{k}) \geq \lambda_{\min}$, where the value of the lower bound $\lambda_{\min} \sim -1/\Delta x^2$ depends on the details of the discretized laplacian. Our stability conditions will rely only on the universal upper bound of zero.

We will use $\lambda(k_x)$ to represent the Fourier transform of the numerical derivative second derivative $\partial^2/\partial x^2$.

3.1. *Euler step*

Our discrete time step, Eq. (2), reduces to an Euler step in the case $b_1 = b_2 = 0$. We plug in $h = x + \eta$ (i.e. slope $C = 1$), linearize in η, and Fourier transform to obtain

$$\tilde{\eta}_{t+\Delta t} = [1 + \Delta t\{-\varepsilon^2 \lambda(\mathbf{k})^2 + 2\lambda(k_x)\}]\tilde{\eta}_t. \tag{12}$$

The vN stability condition is that the square bracket term has magnitude less than unity, to ensure fluctuations die away. The negative curly bracket term in Eq. (12), has no lower bound in the continuum limit $\Delta x \to 0$, and thus the Euler step would be vN unstable for any size Δt. The situation is improved by the numerical derivative, which places a lower bound on the curly bracket terms, leading to vN stability for $\Delta t \lesssim |\lambda_{\min}|^{-2}\varepsilon^{-2} \sim \Delta x^4$. The analysis is essentially identical to what happens in the Cahn–Hilliard equation.[26] The Euler step provides an example of a lattice-dependent stability condition (relying on the lower bound of $\lambda(\mathbf{k})$ rather than the upper bound of zero) and it results in a fixed bound on the time step, regardless of the natural time scale of the dynamics.

3.2. *UvN stability for a single domain*

We return to our parametrized discrete step, Eq. (2), but now we leave b_1 and b_2 unspecified. We seek to find ranges for the parameters which will lift any restrictions on Δt, i.e. unconditional stability. We substitute Eq. (8), with slope $C = 1$ into Eq. (2), linearize, and Fourier transform. The resulting step can be written as

$$[1 + \Delta t\mathcal{L}(\mathbf{k})]\,\tilde{\eta}_{t+\Delta t} = [1 + \Delta t\mathcal{R}(\mathbf{k})]\,\tilde{\eta}_t \tag{13}$$

with

$$\mathcal{L}(\mathbf{k}) = b_1 \lambda(\mathbf{k}) + b_2 \varepsilon^2 \lambda(\mathbf{k})^2 \tag{14}$$

and

$$\mathcal{R}(\mathbf{k}) = 2\lambda(k_x) + b_1 \lambda(\mathbf{k}) + (b_2 - 1)\varepsilon^2 \lambda(\mathbf{k})^2. \tag{15}$$

Before imposing the UvN stability, we note that it is necessary to have $\mathcal{L}(\mathbf{k}) \geq 0$ so that the square bracket on the left of Eq. (13), is nonvanishing for all Δt and $\mathbf{k}$. This gives the requirement that $b_1 \leq 0$ and $b_2 \geq 0$.

Next, the UvN stability condition, $|\tilde{\eta}_{t+\Delta t}| < |\tilde{\eta}_t|$ for all Δt and $\mathbf{k}$, will be satisfied if $\mathcal{L}(\mathbf{k}) > |\mathcal{R}(\mathbf{k})|$. In the case that $\mathcal{R}(\mathbf{k})$ is positive, this gives the condition

$$0 < \mathcal{L}(\mathbf{k}) - \mathcal{R}(\mathbf{k}) = -2\lambda(k_x) + \varepsilon^2\lambda(\mathbf{k})^2, \tag{16}$$

which is intrinsically satisfied due to the nonpositivity of $\lambda(k_x)$. While here and below the $\mathbf{k} = 0$ mode saturates the bound, we can safely ignore it since it is static.

The crucial condition, then, comes from imposing $\mathcal{L}(\mathbf{k}) > -\mathcal{R}(\mathbf{k})$, which becomes

$$\lambda(k_x) + b_1\lambda(\mathbf{k}) + \left(b_2 - \frac{1}{2}\right)\varepsilon^2\lambda(\mathbf{k})^2 > 0. \tag{17}$$

The last term is positive for $b_2 > 1/2$. Next, noting that $\lambda(k_x) \geq \lambda(\mathbf{k})$, we have a lower bound on the remaining two terms:

$$\lambda(k_x) + b_1\lambda(\mathbf{k}) \geq (1 + b_1)\lambda(\mathbf{k}). \tag{18}$$

This will be positive provided that $b_1 < -1$. Thus, our conditions for UvN stability of a single-domain system are

$$b_1 < -1, \quad b_2 > 1/2, \tag{19}$$

which is plotted as the dark gray region of Fig. 1.

Note that for b_1 slightly above -1, in the unstable region, it is Fourier modes with $\lambda(k_x) \approx \lambda(\mathbf{k})$ that first violate Eq. (17). This corresponds to wavevectors $\mathbf{k}$ that are nearly oriented along the x-axis, i.e. the gradient direction of the equilibrium interface.

3.3. *UvN stability for a many-domain system*

In a many-domain system, which is the relevant case for coarsening studies, we are not free to choose the coordinate axes to align the x axis with the interface gradient, since there are many facets with different gradient directions. To analyze this case, we first linearize about a single domain but with an arbitrary normal direction, parametrized by the polar coordinate θ

$$h(x, y, t) = \cos(\theta)x + \sin(\theta)y + \eta(x, y, t). \tag{20}$$

This follows through just as before, with the important stability condition Eq. (17), becoming

$$\cos^2\theta\lambda(k_x) + \sin^2\theta\lambda(k_y) + b_1\lambda(\mathbf{k}) + \left(b_2 - \frac{1}{2}\right)\varepsilon^2\lambda(\mathbf{k})^2 > 0. \tag{21}$$

Now, if many domains are present in the system with essentially random orientations, then for any particular Fourier mode, the above equation will be averaged over θ, giving $\langle\cos^2\theta\rangle = \langle\sin^2\theta\rangle = 1/2$. Using

$$\lambda(k_x) + \lambda(k_y) \approx \lambda(\mathbf{k}) \tag{22}$$

reduces Eq. (21) to

$$\left(b_1 + \frac{1}{2}\right)\lambda(\mathbf{k}) + \left(b_2 - \frac{1}{2}\right)\varepsilon^2\lambda(\mathbf{k})^2 > 0. \tag{23}$$

Thus, our UvN stability condition for many-domain systems is

$$b_1 < -1/2, \quad b_2 > 1/2, \tag{24}$$

which is depicted as the combined shaded regions of Fig. 1. The averaging over multiple orientations provides a greater parameter range of stability than the single-domain case.

Note that in general Eq. (22) is only an approximate relationship. It is a strict equality in the $\Delta x \to 0$ continuum limit, and also in the common five-point stencil for the numerical laplacian on a square lattice, but for other choices of numerical derivatives it need not be exact.

4. Numerical Tests of Energy Stability

Since the field equation of motion is nonlinear, the vN stability analysis is not sufficient to prove energy stability. For that reason, we have conducted extensive numerical tests for energy stability for a range of b_1 and b_2 parameter values. We present the details of the numerical derivative implementation in Sec. 6, but we note here two important general features such an implementation should have. First, the local conservation law should be constructed to hold exactly, without order Δx^n truncation error, and second, the energy-decay property of the continuous time equation should be maintained when spatially discretizing. That is, the particular scheme of calculating the spatially discrete analog of the free energy $F[h]$ in Eq. (6) and the equation of motion should be consistent, so that

$$\frac{d}{dt}h_{ij} = -\frac{\partial}{\partial h_{ij}}\left(\frac{F}{\Delta x^2}\right) \tag{25}$$

is an exact relation, without order Δx^n truncation error.

For each b_1 and b_2 value represented as a data point in Fig. 1, we performed the following tests. First, we nondimensionalize Eq. (2) without loss of generality by rescaling length, height, and time via

$$x \to \varepsilon x' \quad h \to \varepsilon h' \qquad \Delta t \to \varepsilon^2 \Delta t' \quad t \to \varepsilon^2 t'. \tag{26}$$

This transformation results in the same Eq. (2) for the primed quantities with $\varepsilon = 1$. We then evolved 512×512 sized lattices with lattice constant $\Delta x'$ ranging from 0.1 to 1 (or Δx ranging from 0.1ε to ε), up to a final time $t'_{\max}$. These systems were evolved using three different methods: an Euler step with $\Delta t' = 0.003$ out to a $t'_{\max} = 10^4$, a semi-implicit step with $b_1 = -1.5$ and $b_2 = 1$ and growing time step $\Delta t' = 0.003t'^{2/3}$ out to time $t'_{\max} = 10^5$, and the same semi-implicit parameters with a fixed time step $\Delta t' = 10$ out to time $t'_{\max} = 10^5$. For each of these cases,

we analyzed multiple runs and varied between random initial conditions and sinusoidal initial conditions with long and short wavelengths, including the cases studied in Refs. 7, 21. These times may be translated to $\varepsilon \neq 1$ units for any choice of ε by the rescaling $t = \varepsilon^2 t'$.

At regular intervals during the evolution we tested a single step calculated via Eq. (2), with sizes varied between $1 \leq \Delta t' \leq 10^6$. This step was used only for energy stability testing and did not contribute to the subsequent time evolution. Any time that the free energy was found to increase, that particular set of parameter values was identified as unstable.

For the many-domain system, we used periodic boundary conditions and an initially flat interface (plus the random or sinusoidal fluctuations). For the single-domain system, we first re-write the field equation of motion, Eq. (1), in terms of deviations from the uniform slope, giving

$$\frac{\partial \eta}{\partial t} = -\varepsilon^2 \nabla^4 \eta + 2\partial_x^2 \eta + 2\partial_x |\nabla \eta|^2 + 2(\partial_x \eta)\nabla^2 \eta + \nabla \cdot (|\nabla \eta|^2 \nabla \eta), \qquad (27)$$

where $\partial_x = \partial/\partial x$, and then constructed the analogous numerical implementation of this equation. This approach was necessary to eliminate sensitivity to truncation error. We imposed periodic boundary conditions on η, which corresponds to shifted periodic boundary condition on h.

In Fig. 1, we show the results of this testing both for the single- and many-domain systems. The (blue) triangles represent parameter values that were found to be stable for the single-domain system, that is, under all our testing, there were no single incidents of energy increase. The (purple) squares are parameters values that were found to be unstable in the single-domain system, but stable for the many-domain case. The remaining × are parameter values found to be unstable for both single- and many-domain systems. We find a striking degree of agreement between the predictions of UvN stability analysis and the numerical tests for unconditional energy stability. This is one of our main results.

5. Model with Square Symmetry

While the isotropic growth model, Eq. (1), provides a useful starting point for analyzing surface growth coarsening, experimental systems typically select for only a discrete set of slope orientations. For example, homoepitaxial growth on a Cu(100) surface exhibits a square symmetry with four equilibrium slope orientations.[27] This symmetry can be easily added to the phase-field model by adding a term to the free energy functional

$$F_{\text{sq}}[h] = F_{\text{iso}}[h] + \alpha \int d^2x \quad (\partial_x h)^2 (\partial_y h)^2, \qquad (28)$$

where $F_{\text{iso}}[h]$ is the free energy of Eq. (6), α is a nonnegative coefficient determining the strength of the anisotropy, and $\partial_x = \partial/\partial x$. The additional term is nonnegative

and vanishes for slopes oriented with the cartesian axes. For $\alpha = 1$, the potential is isotropic to quadratic order about any of the four equilibrium points.

Taking $\partial h / \partial t = -\delta F_{\mathrm{sq}} / \delta h$ then gives the equation of motion

$$
\begin{aligned}
\frac{\partial h}{\partial t} = {} & -\varepsilon^2 \nabla^4 h - \partial_x \{ [1 - |\nabla h|^2 - 2\alpha(\partial_y h)^2] \partial_x h \} \\
& - \partial_y \{ [1 - |\nabla h|^2 - 2\alpha(\partial_x h)^2] \partial_y h \}.
\end{aligned}
\tag{29}
$$

We parametrize our first-order accurate time step as before, with

$$
h_{t+\Delta t} = h_t + \Delta t \left(\frac{\partial h}{\partial t} \right)_t - b_1 \Delta t \nabla^2 (h_{t+\Delta t} - h_t) - b_2 \varepsilon^2 \Delta t \nabla^4 (h_{t+\Delta t} - h_t). \tag{30}
$$

UvN stability analysis about an equilibrium slope, $h = x + \eta$, takes the same form Eq. (13), with $\mathcal{L}(\mathbf{k})$ unchanged and

$$
\mathcal{R}(\mathbf{k}) = 2(1 - \alpha)\lambda(k_x) + (2\alpha + b_1)\lambda(\mathbf{k}) + (b_2 - 1)\varepsilon^2 \lambda(\mathbf{k})^2. \tag{31}
$$

Following the method of Sec. 3.2 for a single equilibrium domain, the crucial condition $\mathcal{L} + \mathcal{R} > 0$ then results in the stability region

$$
b_1 < -\max(1, \alpha), \quad b_2 > 1/2. \tag{32}
$$

For $\alpha < 1$, the stability boundary is determined by the Fourier mode in the direction of the slope gradient, while for $\alpha > 1$ the boundary is determined by the Fourier mode perpendicular to the slope gradient.

For a multidomain system, we need to average over domains with gradients in the $\pm \hat{x}$ and $\pm \hat{y}$ directions, analogous to the average over orientations in Sec. 3.3.
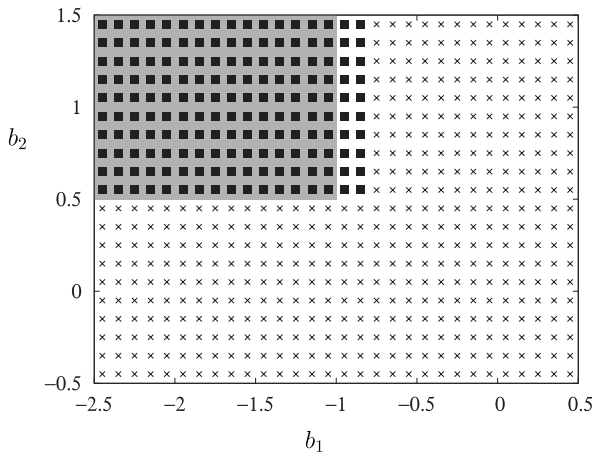

Fig. 2. (Color online) Stability diagram for the square symmetry model of Sec. 5. Squares represent (b_1, b_2) parameter values which were energy stable in our numerical tests, whereas the $\times$ were found to be unstable. The shaded region represents UvN stable parameter values.

This results in the stability region

$$b_1 < -\frac{1+\alpha}{2}, \quad b_2 > 1/2. \tag{33}$$

We conducted numerical tests of energy stability for the multidomain system with $\alpha = 1$ following the same protocol shown in Sec. 4 and again find good agreement, as shown in Fig. 2. The details of our numerical spatial derivatives are provided in Sec. 6.

As this section demonstrates, it is straightforward to generalize the analysis of the isotropic model to the case with a discrete set of preferred slope orientations. In particular, the analysis for models with six-fold symmetry[6] and three-fold symmetry[28] should follow analogously.

6. Finite Difference Scheme

Here, we present details of the spatial discretization scheme we used in our numerical tests. We present these in a discrete-space, continuous time picture, as our goal is to ensure that the conservative dynamics and the gradient flow are exact, i.e. preserved to all orders in Δx. The essential condition for gradient flow is that the equation of motion must be connected to a particular choice for the free energy functional such that

$$\frac{\partial h_{i,j}}{\partial t} = -\frac{\partial}{\partial h_{i,j}}\left(\frac{F}{\Delta x^2}\right). \tag{34}$$

Local conservation is imposed by ensuring that the equation of motion has the form

$$\frac{dh_{i,j}}{dt} = -\frac{1}{\Delta x}[\{J_x\}_{i+1/2,j} - \{J_x\}_{i-1/2,j} - \{J_y\}_{i,j+1/2} - \{J_y\}_{i,j-1/2}] \tag{35}$$

so that the same $\{J_x\}_{i+1/2,j}$ flows into $h_{i+1,j}$ and out of $h_{i,j}$, and the same $\{J_y\}_{i,j+1/2}$ flows into $h_{i,j+1}$ and out of $h_{i,j}$.

Our implementation uses an on-site finite-difference expression for $\nabla^2 h$, for which we take the standard five-point stencil,

$$\{\nabla^2 h\}_{i,j} = \frac{1}{\Delta x^2}[h_{i+1,j} + h_{i-1,j} + h_{i,j+1} + h_{i,j-1} - 4h_{i,j}], \tag{36}$$

and the cell-centered expression for $|\nabla h|^2$,

$$\begin{aligned}\{|\nabla h|^2\}_{i+1/2,j+1/2} = \frac{1}{2\Delta x^2}[&(h_{i+1,j} - h_{i,j})^2 + (h_{i+1,j+1} - h_{i,j+1})^2 \\ + \quad &(h_{i,j+1} - h_{i,j})^2 + (h_{i+1,j+1} - h_{i+1,j})^2].\end{aligned} \tag{37}$$

With these choices, it is straightforward to show that

$$\frac{\partial}{\partial h_{k,l}}\sum_{i,j}\{|\nabla h|^2\}_{i+1/2,j+1/2} = -2\{\nabla^2 h\}_{k,l}. \tag{38}$$

For the isotropic model, our equation of motion is given by Eq. (34), with the choice

$$\frac{F}{\Delta x^2} = \sum_{i,j} \left[\frac{\varepsilon^2}{2} \{\nabla^2 h\}_{i,j}^2 + \frac{1}{4} (1 - \{|\nabla h|^2\}_{i+1/2,j+1/2})^2 \right]. \tag{39}$$

By making use of Eq. (38), the equation of motion can be shown to satisfy the discrete continuity equation (35) with current

$$\{J_x\}_{i+1/2,j} = \{J_x^{\mathrm{SD}}\}_{i+1/2,j} + \{J_x^{\mathrm{NE}}\}_{i+1/2,j}, \tag{40}$$

where the surface diffusion current is

$$\{J_x^{\mathrm{SD}}\}_{i+1/2,j} = \varepsilon^2 \frac{\{\nabla^2 h\}_{i+1,j} - \{\nabla^2 h\}_{i,j}}{\Delta x}, \tag{41}$$

and the nonequilibrium current is

$$\{J_x^{\mathrm{NE}}\}_{i+1/2,j} = \frac{h_{i+1,j} - h_{i,j}}{\Delta x} \\ \times \left[1 - \frac{1}{2} (\{|\nabla h|^2\}_{i+1/2,j+1/2} + \{|\nabla h|^2\}_{i+1/2,j-1/2}) \right], \tag{42}$$

and analogous expressions for $\{J_y\}_{i,j+1/2}$. The discrete form of the free energy, Eq. (39), was used for the numerical tests for energy stability.

For the square symmetry model, we need additionally the cell-centered derivatives

$$\{(\partial_x h)^2\}_{i+1/2,j+1/2} = \frac{1}{2\Delta x^2} [(h_{i+1,j} - h_{i,j})^2 + (h_{i+1,j+1} - h_{i,j+1})^2] \\ \{(\partial_y h)^2\}_{i+1/2,j+1/2} = \frac{1}{2\Delta x^2} [(h_{i,j+1} - h_{i,j})^2 + (h_{i+1,j+1} - h_{i+1,j})^2]. \tag{43}$$

The free energy is given by Eq. (39) with the additional term

$$\frac{F_{\mathrm{sq}}}{\Delta x^2} = \frac{F}{\Delta x^2} + \alpha \sum_{i,j} \{(\partial_x h)^2\}_{i+1/2,j+1/2} \{(\partial_y h)^2\}_{i+1/2,j+1/2}, \tag{44}$$

which corresponds to the nonequilibrium currents

$$\{J_x^{\mathrm{NE,sq}}\}_{i+1/2,j} = \{J_x^{\mathrm{NE}}\}_{i+1/2,j} - \alpha \left(\frac{h_{i+1,j} - h_{i,j}}{\Delta x} \right) \\ \times (\{(\partial_y h)^2\}_{i+1/2,j+1/2} + \{(\partial_y h)^2\}_{i+1/2,j-1/2}), \tag{45}$$

and

$$\{J_y^{\mathrm{NE,sq}}\}_{i,j+1/2} = \{J_y^{\mathrm{NE}}\}_{i,j+1/2} - \alpha \left(\frac{h_{i,j+1} - h_{i,j}}{\Delta x} \right) \\ \times (\{(\partial_x h)^2\}_{i+1/2,j+1/2} + \{(\partial_x h)^2\}_{i-1/2,j+1/2}). \tag{46}$$

7. Coarsening Application

While the isotropic growth model is understood to exhibit $L \sim t^{1/3}$ coarsening, experiments[27] and simulations[6,29] have found $L \sim t^{1/4}$ for crystal growth with square symmetry. However, some variants of this square symmetry model can result in $t^{1/3}$ growth,[30] and more recently, it has been argued that all MBE coarsening with slope selection should asymptotically crossover to $t^{1/3}$ growth, with the observed $t^{1/4}$ behavior being a metastable transient.[8]

As an application, we have simulated the coarsening for both $\alpha = 0$ (isotropic) and $\alpha = 1$ (square symmetry) using the stable step parameters $b_1 = -1.5$ and $b_2 = 1$ and a growing step size

$$\Delta t' = \max(0.1, 0.01 t'^{2/3}) \tag{47}$$

in units with $\varepsilon = 1$, which are generally used in coarsening studies (see, e.g. Refs. 8, 10–13, 24–26, 29). The time t' can be translated to a time t for any value of ε by $t = \epsilon^2 t'$, as in Eq. (26). Shown in Fig. 3 are snapshots of domain configurations for various times for the isotropic model, Eq. (1), simulated on a 512×512 lattice. The analogous configurations for the square symmetry model, Eq. (29), are shown in Fig. 4.

To measure the coarsening rate, we performed 20 independent runs on a 2048×2048 lattice with $\Delta x = \varepsilon = 1$ (which is still small enough to resolve the rounding of

$t' = 1\,000$ $t' = 5\,000$
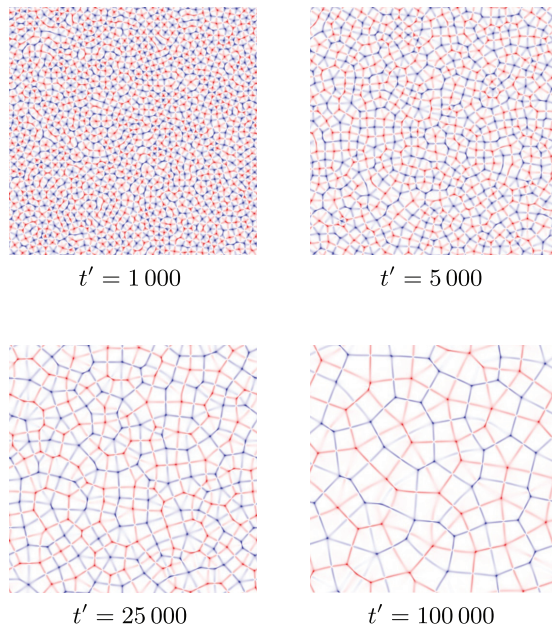
$t' = 25\,000$ $t' = 100\,000$

Fig. 3. (Color online) Plotted is the laplacian of $h(x, y, t)$, for a system evolved with a growing time step $\Delta t \sim t^{2/3}$. Simulation details are provided in the text. Positive values (troughs) are red, negative values (peaks) are blue, and the white regions are domains of uniform slope with zero laplacian.

$t' = 1\,000$ $t' = 5\,000$

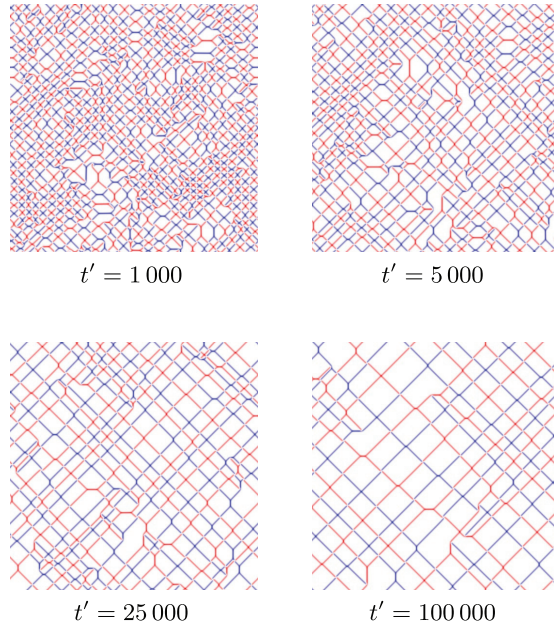$t' = 25\,000$ $t' = 100\,000$

Fig. 4.   (Color online) Plotted is the laplacian of $h(x, y, t)$ as described in Fig. 3, but here for the square symmetry model.

the facet edges), out to time $t'_{\max} = 10^7$. This extends at least two decades farther into the scaling regime than previous simulations. We measure the length scale via the free energy: once equilibrated domains form, the free energy density $f = F/L^2_{\text{sys}}$ is proportional to the amount of edge in the system, which is inversely proportional to the characteristic size of the domains, so $f \sim 1/L(t)$. Figure 5 shows the decay of
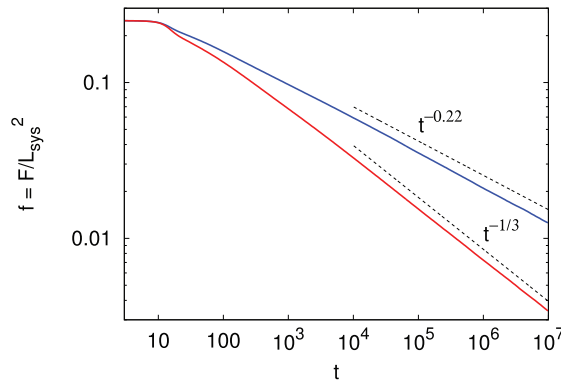

Fig. 5.   (Color online) The free energy density $f = F/L^2_{\text{sys}} \sim 1/L(t)$ as a function of time, where the time evolution utilized a growing time step, $\Delta t \sim t^{2/3}$. Simulation details are in the text. The lower (red) curve is the isotropic model, while the upper (blue) curve is for the anisotropic model with square symmetry.
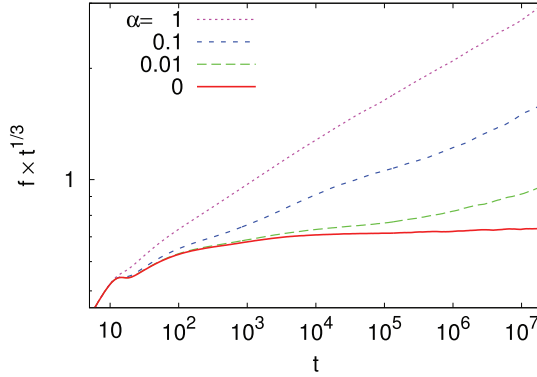
Fig. 6.   (Color online) The free energy density $f = 1/L(t)$ for varying anisotropy strengths α, scaled by the expected $t^{1/3}$ time dependence for the isotropic model. For weak α there is evidence of a crossover from the isotropic to the square-symmetry growth law.

the free energy with time for $\alpha = 0$ (isotropic) and $\alpha = 1$ (square symmetry). For the time range simulated, we observe the expected $t^{1/3}$ growth for the isotropic model, and slightly slower than $t^{1/4}$ growth, with a exponent around 0.22, for the square symmetry model. While these results do not rule out an asymptotic crossover to $t^{1/3}$ growth, we find no signature of the crossover in the extended time range of our simulation.

Next, we explore the hypothesis of a square symmetry to isotropic crossover further by weakening the anisotropy strength α. We measure the growth rates for $\alpha = 0$, 0.01, 0.1 and 1, as shown in Fig. 6, scaled by the expected time dependence of the isotropic model (again measuring the length scale via the free energy density $f \sim 1/L$). We find that for weak α, the dynamics initially tracks the isotropic model, and after sufficient evolution approaches that of the square-symmetry. That is, we see the crossover happen in the opposite direction! Evidently with small enough α, the facets initially form with a nearly isotropic distribution, but the dynamics slowly evolves this towards the square-symmetry distribution over a time scale that varies inversely with α.

8. Summary

We have parametrized a first-order accurate discrete time step for MBE growth with slope selection, given in Eq. (2), that is energy stable for appropriate choices of the parameters b_1 and b_2. We determined the stability range for these parameters via UvN stability analysis, and then tested these predictions with numerical tests for energy stability, as shown in Fig. 1. We find that the UvN stability analysis serves as an accurate proxy for unconditional energy stability, similar to the behavior of the Cahn–Hilliard equation.[12] We extended this analysis to a model with square symmetry, appropriate for growth on a (100) surface.

Our unconditional stability analysis and tests hold for any value of ε, since this parameter can be freely varied by rescaling length and time scales, as in Eq. (26). The accuracy-limited growing step size $\Delta t' = A' t'^{2/3}$ in $\epsilon = 1$ units translates directly to the condition $\Delta t = A t^{2/3}$ for $\epsilon \neq 1$ units, with $A = \epsilon^{2/3} A'$. In particular, the power-law growth of the accuracy-limited time step size is unchanged.

Our stability analysis contained an implicit assumption that the interface slopes do not exceed unit magnitude, which we justify by noting that the dynamics naturally select for this slope. This came into our UvN analysis by our choice to linearize about a unit slope domain. We note that the numerical tests for energy stability contained no such assumption, so the agreement between the two approaches confirms validity of the unit slope assumption. The UvN stability analysis also revealed a distinction in the stability for single-domain and multi-domain interfaces.

The increase in efficiency due to an energy stable method is substantial. For the simulations presented in Fig. 5, computation by Euler step, for which the largest stable step size (in $\varepsilon = 1$ units) is $\Delta t' = 0.03$, would require 3.3×10^8 time steps. In contrast, using a stable method with step size $\Delta t = \max(\Delta t_0, A t^{2/3})$ the number of time steps required to reach some $t_{\max}$ is given by $3 t_{\max}^{1/3} / A$, which for our simulations is 6.5×10^4 steps. Each stable step involves an overhead factor of 2.4 due to the addition of the FFT, but the net result is an overall increase of efficiency by a factor of 2100 for the data we present! Note that this factor will increase as computational resources allow for larger systems to be evolved to later times.

We used this method to extend the range of coarsening simulations for these models by roughly two decades in time. As a result, we found even for weak anisotropy no signature of the recently argued crossover to $t^{1/3}$ coarsening for the square symmetry model.[8]

The method of parametrizing linear semi-implicit steps, performing UvN stability analysis, and then testing the predictions numerically for energy stability has yielded efficient stable methods for the Cahn–Hilliard and Allen–Cahn equations[12] and now for a class of MBE crystal growth models. We anticipate that this procedure will prove useful to many other phase field models.

Acknowledgments

References

1. G. Ehrlich and F. G. Hudda, *J. Chem. Phys.* **44**, 1039 (1966).
2. R. L. Schwoebel and E. J. Shipsey, *J. Appl. Phys.* **37**, 3682 (1966).
3. J. Villain, *J. Phys. I France* **1**, 19 (1991).
4. C. Misbah, O. Pierre-Louis and Y. Saito, *Rev. Mod. Phys.* **82**, 981 (2010).
5. M. Ortiz, E. Repetto and H. Si, *J. Mech. Phys. Solids* **47**, 697 (1999).

6. D. Moldovan and L. Golubovic, *Phys. Rev. E* **61**, 6190 (2000).
7. B. Li and J.-G. Liu, *Euro. J. Appl. Math.* **14**, 713 (2003).
8. S. Biagi, C. Misbah and P. Politi, *Phys. Rev. Lett.* **109**, 096101 (2012).
9. C. Wang, X. Wang and S. M. Wise, *Discret. Contin. Dyn. S.* **28**, 405 (2010).
10. R. V. Kohn and X. Yan, *Comm. Pure App. Math.* **56**, 1549 (2003).
11. A. J. Bray, *Adv. Phys.* **43**, 357 (1994).
12. B. P. Vollmayr-Lee and A. D. Rutenberg, *Phys. Rev. E* **68**, 066703 (2003).
13. M. Cheng and A. D. Rutenberg, *Phys. Rev. E* **72**, 055701 (2005).
14. D. J. Eyre, *MRS Proc.* **529**, 39 (1998).
15. Z. Qiao, Z. Zhang and T. Tang, *SIAM J. Sci. Comput.* **33**, 1395 (2011).
16. W. Chen and Y. Wang, *Numer. Math.* **122**, 771 (2012).
17. J. Shen, C. Wang, X. Wang and S. M. Wise, *SIAM J. Numer. Anal.* **50**, 105 (2012).
18. Z. Qiao, Z. Sun and Z. Zhang, *Numer. Methods Partial Differencial Equations* **28**, 1893 (2012).
19. W. Chen, S. Conde, C. Wang, X. Wang and S. M. Wise, *J. Sci. Comput.* **52**, 546 (2012).
20. W. Chen, C. Wang, X. Wang and S. M. Wise, *J. Sci. Comput.* **59**, 574 (2014).
21. C. Xu and T. Tang, *SIAM J. Numer. Anal.* **44**, 1759 (2006).
22. W. W. Mullins, *J. Appl. Phys.* **30**, 77 (1959).
23. M. D. Johnson, C. Orme, A. W. Hunt, D. Graff, J. Sudijono, L. M. Sander and B. G. Sander, *Phys. Rev. Lett.* **72**, 116 (1994).
24. M. Siegert and M. Plischke, *Phys. Rev. Lett.* **73**, 1517 (1994).
25. M. Rost and J. Krug, *Phys. Rev. E* **55**, 3952 (1997).
26. T. M. Rogers, K. R. Elder and R. C. Desai, *Phys. Rev. B* **37**, 9638 (1988).
27. J. K. Zuo and J. F. Wendelken, *Phys. Rev. Lett.* **78**, 2791 (1997).
28. S. J. Watson and S. A. Norris, *Phys. Rev. Lett.* **96**, 176103 (2006).
29. M. Siegert, *Phys. Rev. Lett.* **81**, 5481 (1998).
30. A. Levandovsky and L. Golubovic, *Phys. Rev. B* **69**, 241402 (2004).